Chemical Science

ROYAL SOCIETY OF CHEMISTRY

EDGE ARTICLE

View Article Online
View Journal

Cite this: DOI: 10.1039/d5sc07909h

All publication charges for this article have been paid for by the Royal Society of Chemistry

Received 13th October 2025
Accepted 18th March 2026

DOI: 10.1039/d5sc07909h

rsc.li/chemical-science

Water self-dissociation in slit pores displays non-monotonic behavior as a function of water filling

Sergi Ruiz-Barragan, *[a] Daniel Muñoz-Santiburcio, [b] Saskia Körning[c] and Dominik Marx [c]

Although nanofluidics and chemistry in nanoconfined liquids has emerged as an exciting field, the quantitative impact of confinement on fundamental properties remains often unclear. Currently, there is not yet consensus on the impact of slit pore confinement on water self-dissociation, namely if this ubiquitous elementary reaction is enhanced, unaltered or suppressed by nanoconfinement. We address this question for well-defined water/graphene slit pore systems that allow us to carefully establish the appropriate thermodynamic conditions for different pore fillings. Anticipating our key results, we show that the energetics of the self-dissociation reaction is very sensitive to even subtle changes of the confinement conditions, leading even to non-monotonic behavior depending on water filling. This effect is found to correlate with the different capabilities of different nanoconfined water lamellae to solvate the nascent hydroxide defect beyond its second hydration shell parallel to the confining walls.

Introduction

Recently, nanoconfined water in different environments has been the focus of intense and growing research efforts[1–3] with the aim to understand its peculiar properties. They include structure and phase behavior,[4–11] dielectric and vibrational spectra,[12–20] dynamics and flow,[21–26] as well as chemical reactivity.[27–36] Regarding the latter, it has become clear that strongly confined water can lead to quite distinct reactivities compared to those in the bulk phase, with immediate interest from electrocatalysis to energy conversion.[37,38]

Much of this peculiar chemistry, on the one hand, certainly appears because of specific interactions between chemically active sites of the confining host material with both, reactant molecules and confined water molecules.[30] But on the other hand, there is evidence that some chemical processes change in confinement compared to bulk because nanoconfined water has different properties from bulk water.[2,36]

Some years ago, we investigated *via* simulations the self-dissociation of nanoconfined water in a layered mineral offering ultranarrow FeS slit pores.[28] The reaction was found to be enhanced in nanoconfinement at high temperature and pressure conditions in comparison to the bulk regime at corresponding conditions. Along the same lines, evidence was provided more recently for the existence of a superionic phase of monolayer water confined between two planar walls at surprisingly low pressure and temperature conditions.[7,57] This peculiar phase of water consists of dissociated molecules and is known to require much higher pressures and temperatures in the bulk regime (of at least about 56 GPa and 700 K).[7] Thus, nanoconfinement of water in narrow slit pores enhances self-dissociation processes at elevated pressure and temperature conditions. Around the same time, is has been discovered[39] that planar confinement of water by graphene or stishovite walls enhances the reactivity of CO_2 with water molecules at high pressure and temperature conditions (of ≈10 GPa and 1000/1400 K), thereby displacing the equilibrium towards the formation of H_2CO_3, HCO_2^- and CO_3^{2-}. Again for CO_2 conversion but now at ambient conditions, nanoconfinement has been demonstrated[33] to not only reduce the reaction free energy barrier as such, as subsequently confirmed also for other geological nanopores,[35] but also that the addition reaction $CO_2 + H_2O$ changes from endo- to exothermic when comparing the bulk reference to confinement scenario. Thus, also this chemical reaction gets enhanced upon nanoconfinement of water. Moreover, strong confinement has been found to facilitate the formation of charged intermediates[33] in line with previous findings in the realm of prebiotic peptide synthesis in nanoconfined water.[27]

Another scenario is found in a recent simulation study[40] addressing water self-dissociation in three graphene-based slit pore setups with different interlayer distances, hosting bi-, tri- and tetra-layer water lamellae at 298 K. This study reports (Fig. 2a therein) that the energy for water self-dissociation increases gradually for water confined between graphene walls upon decreasing their interlayer distance from 1.6 to 1.2 to

[a]Departament de Fisica, Universitat Politécnica de Catalunya, Rambla Sant Nebridi 22, Terrassa 08222, Barcelona, Spain. E-mail: sergio.ruiz.barragan@upc.edu
[b]Instituto Andaluz de Ciencias de la Tierra (IACT-CSIC), Spanish Research Council, Av. de las Palmeras 4, 18100 Armilla, Spain
[c]Lehrstuhl für Theoretische Chemie, Ruhr-Universität Bochum, 44780 Bochum, Germany

0.94 nm. Last but not least, it has been concluded more recently that autoionization of water confined to monolayer lamellae within sub-nanometric slit pores is suppressed.[41] At the molecular level, it is found that this effect can be traced back to the destabilization of the generated hydroxide ion in monolayers due to its restricted hydration therein at interfaces.

Given this variety of scenarios concerning nanoconfinement effects on chemical reactions in general and on water dissociation in graphene slit pores in particular, we set out to resolve this issue. In particular, we quantify the energetic change of this reaction due to nanoscale confinement with slightly different water fillings yet all belonging to the same bilayer stratification regime, while carefully establishing an effective perpendicular pressure in correspondence to the bulk water reference and also monitoring the pressure anisotropy resulting from the inevitable graphene–water interfacial tension effects. Anticipating our key finding, we reveal that water self-dissociation taking place in such narrow slit pores displays a non-monotonic behavior of the corresponding dissociation free energy depending on the filling of the slit pore with water. At the molecular level, this behavior is found to align with distinct differences of the mid-range water structure around the nascent hydroxide defect at both, the lowest and highest water fillings in comparison to the intermediate filling regime.

Methods

Simulation methodology

We employ *ab initio* molecular dynamics (AIMD)[42] for simulating nanoconfined water in graphene slit pores of different equilibrium interlayer distances d_{int} and water fillings at 300 K while explicitly treating all atoms in the system fully consistently at the quantum-mechanical level using the much validated RPBE-D3 density functional.[43,44] We used the CP2K program package,[45–49] throughout to carry out the reported simulations and refer the interested reader to the SI for full details and technical references. We note in passing that this methodology was validated against CCSD(T) reference calculations of graphene–water interactions (see Section I.B in the SI of ref. 5) and, moreover, avoids systematic accuracy problems that easily arise when using force field representations of the graphene sheets, as shown to be particularly severe in the extreme confinement limit as analyzed in Section I.D.2 in the SI of ref. 14. As usual, we compute the free energy for water self-dissociation, ΔF, *via* thermodynamic integration.[42,50,51] This approach is shown to capture well the relative changes of ΔF upon changing the thermodynamic conditions, see SI Section II also for technical aspects.

Piston approach and intrinsic density correction

In order to establish the proper equilibrium interlayer distances depending on water filling, we employ a 'rigid piston approach' where the normal pressure (corresponding to the perpendicular component of the pressure tensor in slit pores) is controlled to establish the desired thermodynamic conditions; we recall that piston approaches are well-established since long to simulate inhomogeneous fluids notably including nanoconfined aqueous solutions as of more recently by others and us.[14,16,41,52–55] In comparison to alternative approaches like coupling slit pores of a fixed width to a bulk water reservoir, piston setups allow one to accurately determine the slit pore width as a function of water filling and also to readily compute the parallel component of the pressure tensor within the confined water slab (using for instance the 'effective pressure tensor' approach[8]). Apart from that, piston approaches avoid the inclusion of a large water reservoir in the simulation cell which would be overly demanding when using full AIMD simulations. However, when the goal is to compare properties of nanoconfined water one-to-one to the bulk water limit, a caveat of the piston approach certainly is that the applied perpendicular pressure must include a correction in order to compensate for density deviations from the experimental bulk water density at a given pressure as used to carry out the bulk reference simulations. In the present case, this 'intrinsic density correction' amounts to an additional 1.6 kbar 'excess piston pressure' which must be applied on top of the desired target pressure (here 1 bar) in order to compensate for the well-known tendency of the RPBE-D3 density functional of slightly underestimating the density of bulk water. These quite technical aspects when simulating confined liquids at controlled anisotropic pressure conditions using piston approaches, notably nanoconfined water in graphene-based slit pores, are explained in more detail in the present SI Section I.D. For even deeper discussions and analyses we refer the interested reader to SI Section I.E of ref. 14 for general background while the corresponding AIMD simulation methodology has been introduced and validated in SI Section II.D of ref. 16.

Pressure anisotropy

Before proceeding, we must address the intricate problem of determining the proper solvent filling of narrow slit pores that corresponds to desired thermodynamic (T, p) conditions corresponding to bulk reference data at a comparable thermodynamic state point; we refer to ref. 8 for a broad introduction into this issue including background references.

Fundamentally, it must be recognized that while bulk water is a homogeneous liquid with isotropic properties, confined water is inhomogeneous and presents anisotropic properties. This is also the case of the pressure, which is a tensorial property in slit pores as opposed to a scalar one in bulk. In particular, the coplanar nature of this confining setup causes a well-defined difference between the perpendicular and parallel pressure tensor components.[56] This difference is directly determined by the interfacial tension, which is a thermodynamic property that depends on the confined liquid as well as on the confining material and on the pore geometry.

Recently,[8] we have shown that even when controlling the perpendicular pressure, slightly different pore fillings lead to vastly different values of the effective parallel pressure, $\mathbf{P}_{\parallel}^{\mathrm{eff}}$. For bilayer water in graphene slit pores, however, we found that there exist distinct conditions where the effective pressure tensor of nanoconfined water is isotropic. Therefore, at this specific state

point, the pressure of the inhomogeneous fluid in the slit pore is effectively a scalar property as it fundamentally is in the corresponding homogeneous fluid, bulk water. This well-defined point of vanishing effective interfacial tension is the natural reference state to compare the properties of nanoconfined fluids to those of the corresponding bulk fluid at the same (effectively isotropic) pressure condition and the same temperature.[8]

Results and discussion

Interlayer distance *versus* pore filling

Here, we use the rigid piston approach in the framework of fully consistent AIMD simulations.[42] Thus including all water molecules as well as the graphene walls on equal footing to compute the equilibrium interlayer distances $\langle d_{\mathrm{int}} \rangle$ at the same perpendicular pressure that reproduces the experimental density of water at 1 bar and 300 K in the bulk liquid reference phase. This is done for water fillings (reported in area number densities: H_2O per Å^2) that span regimes from monolayer to bilayer to trilayer water lamellae at smallest, intermediate and largest fillings, see Fig. 1. The flat monolayer regime extends until fillings of about 0.115 H_2O per Å^2, when further filling leads to a somewhat corrugated monolayer, and later to a disordered/incomplete bilayer, which gradually becomes sharply defined until reaching 0.216 H_2O per Å^2 (system V). Adding only a little more water beyond this point suddenly leads to the loss of the sharp bilayer stratification, yielding two diffuse external layers bridged by "intermediate' molecules" (system VI).

Here, we will focus exclusively on the stratified bilayer regime, which as seen in Fig. 1 can be sampled by analyzing five slit pores with water fillings of 0.152, 0.165, 0.182, 0.199, 0.216 H_2O per Å^2 corresponding to the slit pore setups (I) to (V). Those yield equilibrium interlayer distances of $\langle d_{\mathrm{int}} \rangle = 9.02$, 9.25, 9.41, 9.54, and 9.67 Å as computed from rigid piston simulations by averaging over the fluctuating interlayer distances d_{int} at each state point. It is worth noting that within this stable bilayer region, $\langle d_{\mathrm{int}} \rangle$ is found to only mildly increase.

For each of these systems, we fixed the interlayer distance at the consistently computed equilibrium value $\langle d_{\mathrm{int}} \rangle$ thus continuing the AIMD simulations with the frozen piston method[14,16] to compute the corresponding free energy for water self-dissociation, ΔF, as a function of pore filling (as detailed in the SI). In addition, for each slit pore setup with its frozen equilibrium interlayer distance depending on pore filling, we calculated $\mathbf{P}_{\parallel}^{\mathrm{eff}}$ as also described in the SI, while $\mathbf{P}_{\perp}^{\mathrm{eff}}$ is given by the normal pressure corresponding to the piston pressure.

Non-monotonic water self-dissociation in bilayers

The free energy barriers for the water self-dissociation reaction at 300 K in the selected slit pores, together with that for the bulk reference at 300 K and 1 bar, are compiled in Fig. 2 (while the full free energy profiles determined *via* constrained AIMD are

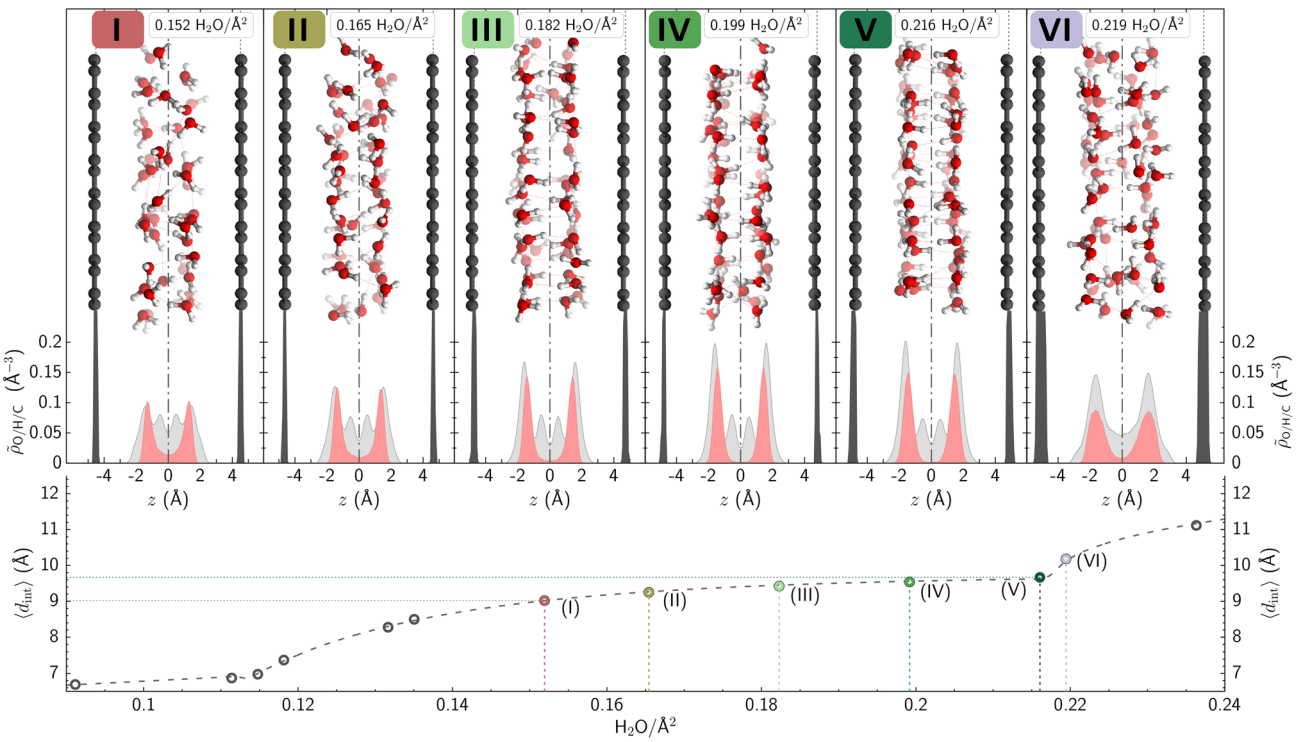

Fig. 1 Equilibrium interlayer distances, $\langle d_{\mathrm{int}} \rangle$, of water-filled graphene slit pores at 300 K at a perpendicular pressure corresponding to 1 bar at 300 K (determined from rigid piston AIMD simulations by applying a constant excess piston pressure of 1.6 kbar to consider the intrinsic density correction, we refer the interested reader to the main text and the SI for background and details) as a function of pore filling given by the area number densities of water (*i.e.* H_2O per Å^2, see text). The circles are the AIMD data while the interpolating dashed line is merely a guide to the eye. Top figures: Average perpendicular number density profiles (red: O, clear gray: H, black: C) for selected area number densities as reported therein and highlighted by filled circles in the main graph with I, II, III, IV, V, VI.

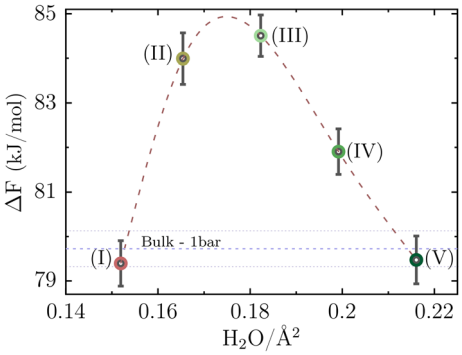

Fig. 2 Free energy for water self-dissociation, ΔF, of bilayer water at 300 K confined in graphene slit pores at a perpendicular pressure corresponding to 1 bar at 300 K (thus at constant excess piston pressure of 1.6 kbar to consider the intrinsic density correction, see text and SI) for slit pore setups (I) to (V) using the consistent fixed equilibrium interlayer distances, $\langle d_{\mathrm{int}} \rangle$, as a function of pore filling, H_2O per Å^2, see text. The circles with error bars are the AIMD data while the interpolating natural cubic spline fit (long dashed line) is merely a guide to the eye. The reference dissociation free energy corresponding to bulk water at 1 bar and 300 K (also subject to the intrinsic density correction) is included as a horizontal dashed line with the error bar reported by horizontal dotted lines. The error bars were estimated based on block averaging of the full trajectories in terms of four statistically independent pieces.

shown in the SI). These ΔF values are, in the first place, sensitive to the nanoscale environment as provided by the different slit pore bilayer setups (I) to (V) according to the data in Fig. 2.

Secondly and maybe more interestingly, these free energies are found to feature a non-monotonic behavior as a function of slit pore filling. This effect is non-negligible since it amounts to free energy changes of about 5 kJ mol^{-1} overall (thus being a nanoconfinement phenomenon that is clearly outside the mutual error estimates across the fillings) upon seemingly minor modifications of the stratified water structure in the bilayer, see the snapshots and perpendicular density profiles (I) to (V) in Fig. 1. In particular, an increase in $\langle d_{\mathrm{int}} \rangle$ as small as 0.4 Å from slit pore (I) to (III) corresponds to an enhancement of ΔF by about 5 kJ mol^{-1}, while another increase of only 0.25 Å from setup (III) to (V) corresponds to a decrease of ΔF again by 5 kJ mol^{-1} in conjunction with the underlying changes of slit pore fillings.

Thirdly, the computed dissociation barriers depending on water filling are such that two of the slit pores, namely setups (I) and (V) feature a small decrease of the free energy for water self-dissociation compared to the bulk reference, thus corresponding to a slightly enhanced reaction. In contrast, the self-dissociation reaction is disfavored for bilayers at intermediate water fillings. We also note that the effective parallel pressures are mostly strongly negative by several kbar, see Fig. S4 in the SI. However, in case of system (V) with an area number density of 0.216 H_2O per Å^2, which corresponds to the upper limit of the stable bilayer domain as the filling increases, indeed provides a nearly isotropic effective pressure tensor.

Molecular-level picture

Is there a way to provide molecular insights that might explain the unveiled non-monotonic behavior of the self-dissociation barriers as a function of water filling being highest at the three intermediate area number densities but lower than the bulk reference value at both, the lowest and highest densities? Upon comprehensive analyses, we found that the mid-range hydration water structure around the nascent OH^- ion features subtle qualitative differences depending on water filling, where 'mid-range' refers here to $OH^-\cdots H_2O$ pair correlations beyond the second hydration shell of OH^- parallel to the graphene walls. The three intermediate fillings corresponding to setups (II), (III) and (IV) feature pronounced mid-range hydration of OH^- with interfacial water close to the graphene walls, while hydration of OH^- at mid-range

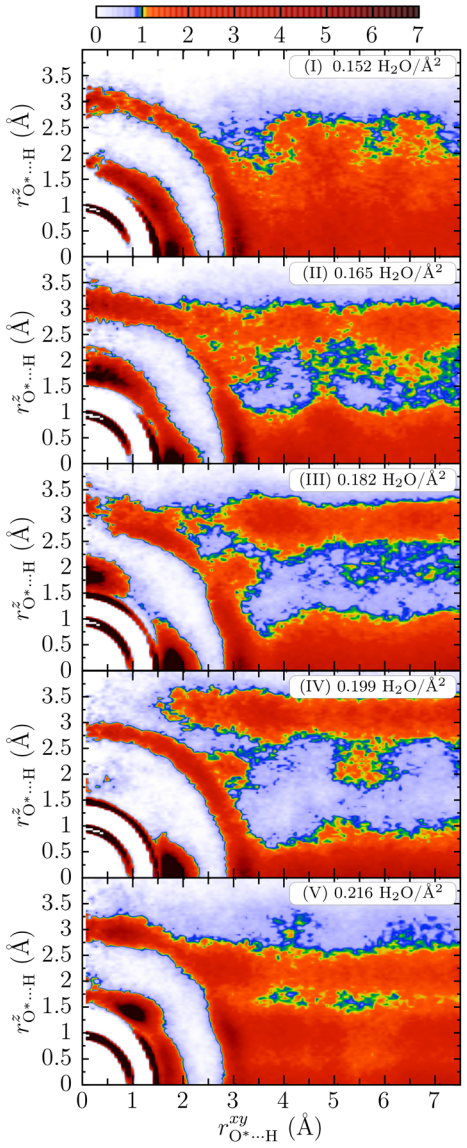

Fig. 3 Two-dimensional pair correlation functions of the water hydrogen atoms with respect to the oxygen atom O* of the dissociating water molecule giving rise to the nascent O*H$^-$ (based on the trajectories obtained using the coordination number $CN_{O^*,H} = 1.3$ at which ΔF in Fig. 2 is determined from thermodynamic integration as described in SI Section I.C). The color code (top bar) quantifies the value of $g^{2D}(r^z_{O^*H}, r^{xy}_{O^*H})$ at the respective O*$\cdots$H distances along the z axis and within the xy plane, *i.e.* perpendicular and parallel to the graphene walls; note that green corresponds to $g \approx 1$.

distances is greatly suppressed in the central region of these slit pores. In stark contrast, the limiting low- and high-density fillings (I) and (V) display, both, uniform and pronounced mid-range hydration of OH^-.

This qualitative picture has been extracted by going beyond analyses of spherically averaged radial distribution functions with respect to OH^- or its local H-bonding properties. To this end, we consider the perpendicular and parallel anisotropy of the nanoconfined water lamellae as imprinted by the two coplanar graphene walls by employing a two-dimensional pair correlation function $g^{2D}(r^z_{O^*H},\ r^{xy}_{O^*H})$ as depicted in Fig. 3 for the five slit pore fillings; note that the quarter-circular structures at distances of about 1 Å corresponds to the intramolecular O*H covalent bond in OH^- itself.

At the lowest and highest water fillings (top and bottom panels of Fig. 3, respectively), the region beyond the second hydration shell of OH^- is characterized by an extended and homogeneous red area (where $g \gg 1$) without much modulations that corresponds to a high water probability density throughout at these distances relative to OH^-. This implies that OH^- is very well embedded in solvation water in the two nanoconfined water lamellae corresponding to setups (I) and (V) at mid-range $OH^-\cdots$water distances.

The scenario in the three slit pores with intermediate water area number densities, as provided by the setups (II), (III) and (IV), is found to be distinctly different according to Fig. 3. At mid-range O*$\cdots$H distances there is a spacious blue basin that is limited by two rather narrow red horizontal stripes at the top and bottom. This implies very low (blue: $g \ll 1$) and high (red: $g \gg 1$) water probability densities w.r.t. OH^-, respectively, in these well-separated regions across the slit pores. Thus, in contrast to the two extremely low and high water fillings, the three slit pores with intermediate water area number density are subject to highly modulated and most stratified solvation water environments in the mid-distance range. Therefore, OH^- cannot be well solvated by mid-ranged water molecules throughout slit pores (II), (III) and (IV).

Overall, we find that the nascent OH^- species are very well embedded in hydration water at distances beyond its second solvation shell only in the narrowest and widest slit pores with lowest and highest water filling, respectively. These are the two slit pores (I) and (V) that provide the lowest self-dissociation free energy ΔF according to Fig. 2. In contrast, the slit pores with intermediate water fillings, which lead to nanoconfined water lamellae where OH^- cannot be well solvated parallel to the walls by water molecules beyond the second solvation shell. This restriction of mid-range hydration of OH^- consistently correlates with higher free energy barriers for water self-dissociation within nanoconfined water lamellae.

Conclusions and outlook

Given controversial conclusions in the recent literature on nanoconfinement effects on pure water, we carefully investigated the free energy barrier for water self-dissociation in well-defined slit pore setups which host bilayer water lamellae between two coplanar graphene walls at room temperature. First of all, our data unveil that there exists an extended stability domain of bilayer water at 300 K at a constant normal pressure corresponding to 1 bar in terms of water filling in conjunction with the corresponding equilibrium graphene-to-graphene interlayer distance which determines the nanoscale confinement. Secondly, we find that the free energy barrier of water self-dissociation in this bilayer regime does critically depend on slit pore setup and water filling. Therefore, our quantitative data demonstrate that the self-dissociation reaction of water is surprisingly sensitive to subtle details of the nanoconfinement conditions.

Regarding the more specific question of whether self-dissociation of water in slit pores is either enhanced, unaltered or suppressed by nanoconfinement with respect to the bulk regime, the answer is that it very delicately depends on the particular filling and interlayer distance of the pore. As we have demonstrated, quite subtle changes in the slit pore setup, as small as roughly 0.3–0.4 Å in interlayer distances in conjunction with the corresponding equilibrium water fillings, involve a change in the dissociation barrier of about 5–6 kJ mol^{-1} either way with the highest barrier occurring at intermediate fillings. Thus, the dissociation reaction can be either significantly disfavored (at intermediate water fillings) or slightly enhanced (at the lowest and highest fillings) with respect to bulk water.

Having disclosed such non-monotonic behavior of the self-dissociation barrier of nanoconfined water as a function of slit pore filling, we found that this phenomenon aligns with differences in hydration of the nascent hydroxide defect beyond its second solvation sphere that depends on the respective water lamellae. High free energy barriers are found for slit pores with intermediate water fillings: they lead to nanoconfined water lamellae where OH^- cannot be well solvated parallel to the walls by water molecules beyond the second solvation shell. Thus, for such fillings, hydration of OH^- beyond its second solvation shell is restricted in major regions within these slit pores. Low free energy barriers, instead, correlate with lamellae that allow for pronounced and uniform hydration of OH^- beyond its second solvation shell, which offers comprehensive embedding of OH^- in the H-bond network of these nanoconfined water lamellae.

In future research, the impact of different thermodynamic state points in terms of temperature and pressure conditions beyond ambient might be interesting to be explored, including the aforementioned high temperature and pressure conditions addressed in some previous work. Another research direction certainly is to study systematically chemical reactions other than water self-dissociation by using such well-defined slit pore setups. Together, these insights will pave the path for exploiting nanoconfined water as a versatile ecosystem to enhance or suppress specific chemical reactions using nanofluidic devices.

Author contributions

Conceptualization and methodology: SRB, DMS, DM; software: SRB, DMS, SK; validation: SRB, DMS; formal analysis and investigation: SRB, DMS, SK; writing – original draft: SRB, DMS, DM; writing – review & editing: SRB, DMS, DM; visualization:

SRB; supervision, project administration and funding acquisition: SRB, DMS, DM.

Conflicts of interest

There are no conflicts to declare.

Data availability

Data available on request from the corresponding author.

Supplementary information (SI): computational details (simulation, models, methodology), validation of methodology, full free energy profiles and effective parallel pressure. See DOI: https://doi.org/10.1039/d5sc07909h.

Acknowledgements

This work was supported by the Research Training Group "Confinement-controlled Chemistry" funded by the Deutsche Forschungsgemeinschaft (DFG, German Research Foundation) under grant GRK 2376/331085229. Also funded by DFG under Germany's Excellence Strategy – EXC 2033 – 390677874 – RESOLV as well as by the individual M. Zambrano grant 2021UPC-MZ-67522 to SR-B, and Grant RYC2023-045757-I funded by MICIU/AEI/10.13039/501100011033 and ESF+ to DM-S. Computing resources have been provided by Leibniz-Rechenzentrum München (SuperMUC and SuperMUC–NG), HPC@ZEMOS, HPC–RESOLV, and BOVILAB@RUB.

Notes and references

1 L. Bocquet, *Nat. Mater.*, 2020, **19**, 254–256.
2 D. Muñoz-Santiburcio and D. Marx, *Chem. Rev.*, 2021, **121**, 6293–6320.
3 M. Jaugstetter, N. Blanc, M. Kratz and K. Tschulik, *Chem. Soc. Rev.*, 2022, **51**, 2491–2543.
4 G. Algara-Siller, O. Lehtinen, F. Wang, R. Nair, U. Kaiser, H. Wu, A. Geim and I. Grigorieva, *Nature*, 2015, **519**, 443–445.
5 S. Ruiz-Barragan, D. Muñoz-Santiburcio and D. Marx, *J. Phys. Chem. Lett.*, 2019, **10**, 329–334.
6 Z. Gao, N. Giovambattista and O. Sahin, *Sci. Rep.*, 2018, **8**, 6228.
7 V. Kapil, C. Schran, A. Zen, J. Chen, C. J. Pickard and A. Michaelides, *Nature*, 2022, **609**, 512–516.
8 S. Ruiz-Barragan, H. Forbert and D. Marx, *Phys. Chem. Chem. Phys.*, 2023, **25**, 28119–28129.
9 K. D. Fong, B. Sumić, N. O'Neill, C. Schran, C. P. Grey and A. Michaelides, *Nano Lett.*, 2024, **24**, 5024–5030.
10 F. Della Pia, A. Zen, V. Kapil, F. L. Thiemann, D. Alfè and A. Michaelides, *J. Chem. Phys.*, 2024, **161**, 224706.
11 X. R. Advincula, K. D. Fong, A. Michaelides and C. Schran, *ACS Nano*, 2025, **19**, 17728–17737.
12 L. Fumagalli, A. Esfandiar, R. Fabregas, S. Hu, P. Ares, A. Janardanan, Q. Yang, B. Radha, T. Taniguchi, K. Watanabe, G. Gomila, K. S. Novoselov and A. K. Geim, *Science*, 2018, **360**, 1339–1342.
13 P. Loche, C. Ayaz, A. Schlaich, D. J. Bonthuis and R. R. Netz, *J. Phys. Chem. Lett.*, 2018, **9**, 6463–6468.
14 S. Ruiz-Barragan, D. Muñoz-Santiburcio, S. Körning and D. Marx, *Phys. Chem. Chem. Phys.*, 2020, **22**, 10833–10837.
15 F. Deißenbeck, C. Freysoldt, M. Todorova, J. Neugebauer and S. Wippermann, *Phys. Rev. Lett.*, 2021, **126**, 136803.
16 S. Ruiz-Barragan, F. Sebastiani, P. Schienbein, J. Abraham, G. Schwaab, R. R. Nair, M. Havenith and D. Marx, *Phys. Chem. Chem. Phys.*, 2022, **24**, 24734–24747.
17 B. Das, S. Ruiz-Barragan and D. Marx, *J. Phys. Chem. Lett.*, 2023, **14**, 1208–1213.
18 S. Mondal and B. Bagchi, *J. Chem. Phys.*, 2024, **161**, 220901.
19 M. R. Becker and R. R. Netz, *J. Chem. Phys.*, 2024, **161**, 224704.
20 T. Dufils, C. Schran, J. Chen, A. K. Geim, L. Fumagalli and A. Michaelides, *arXiv*, 2025, preprint, arXiv:2211.14035v1, Version 1, DOI: 10.48550/arXiv.2211.14035.
21 G. Hummer, J. C. Rasaiah and J. P. Noworyta, *Nature*, 2001, **414**, 188–190.
22 E. Secchi, S. Marbach, A. Niguès, D. Stein, A. Siria and L. Bocquet, *Nature*, 2016, **537**, 210–213.
23 M. Neek-Amal, F. M. Peeters, I. V. Grigorieva and A. K. Geim, *ACS Nano*, 2016, **10**, 3685–3692.
24 F. L. Thiemann, C. Schran, P. Rowe, E. A. Müller and A. Michaelides, *ACS Nano*, 2022, **16**, 10775–10782.
25 B. Das, S. Ruiz-Barragan, B. Bagchi and D. Marx, *Nano Lett.*, 2024, **24**, 15623–15628.
26 K. D. Fong, C. P. Grey and A. Michaelides, *ACS Nano*, 2025, **19**, 13191–13201.
27 D. Muñoz-Santiburcio and D. Marx, *Chem. Sci.*, 2017, **8**, 3444–3452.
28 D. Muñoz Santiburcio and D. Marx, *Phys. Rev. Lett.*, 2017, **119**, 056002.
29 L. R. Pestana, H. Hao and T. Head-Gordon, *Nano Lett.*, 2019, **20**, 606–611.
30 A. B. Grommet, M. Feller and R. Klajn, *Nat. Nanotechnol.*, 2020, **15**, 256–271.
31 D. T. Bregante, M. C. Chan, J. Z. Tan, E. Z. Ayla, C. P. Nicholas, D. Shukla and D. W. Flaherty, *Nat. Catal.*, 2021, **4**, 797–808.
32 J. Fortunato, J. W. Jordan, G. N. Newton, D. A. Walsh and V. Augustyn, *Curr. Opin. Electrochem.*, 2022, **34**, 101014.
33 N. Dasgupta, T. A. Ho, S. B. Rempe and Y. Wang, *J. Phys. Chem. Lett.*, 2023, **14**, 1693–1701.
34 H. Dai, N. Li, J. Ye, J. Zhao, X. He, X. Duan, B. Yan, G. Chen and S. Wang, *Chem. Eng. J.*, 2023, 144861.
35 N. Dasgupta, T. A. Ho, S. B. Rempe and Y. Wang, *J. Phys. Chem. C*, 2024, **128**, 5878–5888.
36 T. Wang, H. Iriawan, J. Peng, R. R. Rao, B. Huang, D. Zheng, D. Menga, A. Aggarwal, S. Yuan, J. Eom, Y. Zhang, K. McCormack, Y. Román-Leshkov, J. Grossman and Y. Shao-Horn, *Chem. Rev.*, 2025, **125**, 1420–1467.
37 T. A. Shifa and A. Vomiero, *Adv. Energy Mater.*, 2019, **9**, 1902307.
38 J. Zhou, M. Zhang, Y. Lin, J. Xu, C. Pan, Y. Lou, Y. Zhang, Y. Wang, Y. Dong, Y. Zhu, J. Zhang and Z. Lin, *Nano Energy*, 2024, **125**, 109529.

39 N. Stolte, R. Hou and D. Pan, *Nat. Commun.*, 2022, **13**, 5932.
40 S. Di Pino, Y. A. Perez Sirkin, U. N. Morzan, V. M. Sanchez, A. Hassanali and D. A. Scherlis, *Angew. Chem., Int. Ed.*, 2023, **62**, e202306526.
41 S. Dasgupta, S. Saha and F. Paesani, *J. Am. Chem. Soc.*, 2025, **147**, 25167–25173.
42 D. Marx and J. Hutter, *Ab Initio Molecular Dynamics: Basic Theory and Advanced Methods*, Cambridge University Press, 2009.
43 B. Hammer, L. B. Hansen and J. K. Nørskov, *Phys. Rev. B: Condens. Matter Mater. Phys.*, 1999, **59**, 7413–7421.
44 S. Grimme, J. Antony, S. Ehrlich and H. Krieg, *J. Chem. Phys.*, 2010, **132**, 154104.
45 J. VandeVondele, M. Krack, F. Mohamed, M. Parrinello, T. Chassaing and J. Hutter, *Comput. Phys. Commun.*, 2005, **167**, 103–128.
46 J. Hutter, M. Iannuzzi, F. Schiffmann and J. VandeVondele, *Wiley Interdiscip. Rev. Comput. Mol. Sci.*, 2014, **4**, 15–25.
47 T. D. Kühne, M. Iannuzzi, M. Del Ben, V. V. Rybkin, P. Seewald, F. Stein, T. Laino, R. Z. Khaliullin, O. Schütt, F. Schiffmann, D. Golze, J. Wilhelm, S. Chulkov, M. H. Bani-Hashemian, V. Weber, U. Borštnik, M. Taillefumier, A. S. Jakobovits, A. Lazzaro, H. Pabst, T. Müller, R. Schade, M. Guidon, S. Andermatt, N. Holmberg, G. K. Schenter, A. Hehn, A. Bussy, F. Belleflamme, G. Tabacchi, A. Glöß, M. Lass, I. Bethune, C. J. Mundy, C. Plessl, M. Watkins, J. VandeVondele, M. Krack and J. Hutter, *J. Chem. Phys.*, 2020, **152**, 194103.
48 M. Iannuzzi, J. Wilhelm, F. Stein, A. Bussy, H. Elgabarty, D. Golze, A.-S. Hehn, M. Graml, S. Marek, B. Sertcan Gökmen, C. Schran, H. Forbert, R. Z. Khaliullin, A. Kozhevnikov, M. Taillefumier, R. Meli, M. B. V. V. Rybkin, R. Schade, O. Schütt, J. V. Pototschnig, H. Mirhosseini, A. Knüpfer, D. Marx, M. Krack, J. Hutter and T. D. Kühne, *J. Phys. Chem. B*, 2026, **130**, 1237–1310.
49 CP2K Open Source Molecular Dynamics, https://www.cp2k.org/.
50 E. Carter, G. Ciccotti, J. T. Hynes and R. Kapral, *Chem. Phys. Lett.*, 1989, **156**, 472–477.
51 M. Sprik and G. Ciccotti, *J. Chem. Phys.*, 1998, **109**, 7737–7744.
52 S. Gekle and R. R. Netz, *J. Chem. Phys.*, 2012, **137**, 104704.
53 R. Richard, S. Anthony and G. Aziz, *Mol. Phys.*, 2016, **114**, 2655–2663.
54 M. Yang, Q. Sheng, L. Guo, H. Zhang and G. Tang, *Langmuir*, 2022, **38**, 2238–2247.
55 M.-L. Tseng, A. Adesiyan, A. Gassoumi and N. E. Gorji, *J. Nanoparticle Res.*, 2023, **25**, 51.
56 J. G. Kirkwood and F. P. Buff, *J. Chem. Phys.*, 1949, **17**, 338–343.
57 V. Kapil, C. Schran, A. Zen, J. Chen, C. J. Pickard and A. Michaelides, *Nature*, 2025, **648**, E15.